A magneto-spectroscopic study of epitaxial graphene

Sven Deutschländer

9th July 2008

Report to a practical semester, supervised by

Prof. Dr. Georg Maret (University of Konstanz),
Dr. Gérard Martinez (LCMI Grenoble),
Dr. Milan Orlita (LCMI Grenoble).

Contents

1 Introduction 2

2 Basic theory of graphene 3
- 2.1 The lattice structure . . . 3
- 2.2 The band structure . . . 4
- 2.3 Magnetic properties . . . 6
- 2.4 Epitaxial graphene . . . 7

3 Experimental setup 8
- 3.1 The spectrometer . . . 8
- 3.2 The magnets . . . 10
- 3.3 Basic measurement and beam alignment . . . 10

4 Experiments 12
- 4.1 The samples . . . 12
- 4.2 Infrared transmission studies . . . 12
- 4.3 Raman scattering studies . . . 16
- 4.4 Transmittance of the new samples . . . 17
- 4.5 Conclusions . . . 20

5 Thanks 21

1 Introduction

This report completes a stage of intensive experimental studies in the field of solid state physics, performed at the Laboratoire des Champs Magnétiques Intenses (LCMI), CNRS, Grenoble. The stage is a practical semester, authorized by the University of Konstanz. It gave the author the opportunity to spend twenty weeks in a research or working group of an institute, university or company, in the home or a foreign country, to get introduced into the working life of a scientist. The purpose is not only to learn practical methods of research and manufacturing, but also to help the student to decide, what career path he wants to pursue in the future. The practical semester is involved in the study course of the university and therefore the student has to bear witness in form of a report, including the theoretical background and the practical work of his studies.

The LCMI is the high magnetic field laboratory of Grenoble (GHMFL), and part of the Centre National de la Recherche Scientifique (CNRS). The laboratory is running eight resistive magnets, which can be used by the local groups as well as by foreign researchers. In addition superconducting coils and experimental setups for optical measurements are available. The local groups are doing research in electron paramagnetic resonance (EPR), nuclear magnetic resonance (NMR), mesoscopic physics and investigate magnetic and optical properties of metals, superconductors and semiconductors. The laboratory possesses its own technical section which develops the magnets and the cryogenic setup and provides the electronic systems.

The author worked within the semiconductor group, who performs transport measurements, optical and infrared spectroscopy. He was involved, together with Gérard Martinez and Milan Orlita, in a project to investigate electronic and optical properties of certain graphene samples, which included

- investigations of infrared transmission in a two-dimensional electron gas
- working with a Fourier transform spectrometer
- measuring in high magnetic fields and at low temperatures
- performing Raman spectroscopy
- the evaluation of experimental data

and of course the opportunity to work with international researchers to improve language skills and the ability to work within a team. In addition, the author had the chance to join various seminars, which generally take place in the laboratory once a week. As a conclusion, the practical semester was a great experience for the author, who enjoyed this stage in a professional as well as in a personal sense.

2 Basic theory of graphene

In this section the basic theory will be discussed. We start with basic considerations about the lattice symmetry. In addition the band structure will be presented, as well as the magnetic properties. In the end some considerations about the way of producing graphene will be made.

2.1 The lattice structure

In graphene three of the four valence electrons of the carbon atom are performing a sp^2-hybridization, which consists of three linear combinations of one 2s state and two 2p states perpendicular to each other. These σ-bands perform very strong bonds in plane to the neighbor atoms, by overlapping with other σ-bands, building a honeycomb lattice, where the electron bonds are arranged with an angle of 120° to each other. The fact that the bonding energy of the σ-bands is big compared to the energy difference between the 2s and the 2p level gives rise to this superposition of eigenstates. The remaining electron remains in a 2p state perpendicular to the ones in the hybridization, called π-band, and overlaps with the π-bands of the neighbor atoms. If we assume, that the lattice is in the xy plane and put one of the σ-bands parallel to the y-axis, they should satisfy the directions (0, -1, 0), ($\sqrt{3}/2$, 1/2, 0) and (-$\sqrt{3}/2$, 1/2, 0). Since the hybridized states are orthogonal, the corresponding conditions $\langle \psi_i | \psi_j \rangle = \delta_{ij}$, with the Kronecker δ, to determine the constants of the linear combinations, and the given directions lead to the three σ-bands $|sp_a^2\rangle = (1/\sqrt{3})|2s\rangle - \sqrt{2/3}|2p_y\rangle$, $|sp_b^2\rangle = (1/\sqrt{3})|2s\rangle + (1/\sqrt{2})|2p_x\rangle + (1/\sqrt{6})|2p_y\rangle$, $|sp_c^2\rangle = -(1/\sqrt{3})|2s\rangle - (1/\sqrt{2})|2p_x\rangle + (1/\sqrt{6})|2p_y\rangle$ and the π-band $|2p_z\rangle$[12]. Looking closer to the given lattice structure, shown in figure 1 (a), we can clearly see that the carbon atoms are not building a Bravais lattice, since, by starting at one atom, the coordinates of all other atoms can not be found by a translation of the form $\vec{T} = n \cdot \vec{a_1} + m \cdot \vec{a_2}$ $(n, m \in Z)$ with arbitrarily chosen but fixed vectors a_1 and a_2. With this follows, that the unit cell, which must satisfy the whole symmetry of the lattice by translations given above, includes two inequivalent atoms A and B. The lattice vectors are

$$\vec{a_1} = \left(\frac{\sqrt{3}}{2} a, \frac{a}{2} \right), \quad \vec{a_2} = \left(\frac{\sqrt{3}}{2} a, -\frac{a}{2} \right), \tag{1}$$

where a is the distance of two atoms of type A or B,

$$a = |\vec{a_1}| = |\vec{a_2}| = \sqrt{3} \cdot a_{C-C} = 0.246\text{nm}^{[11]}. \tag{2}$$

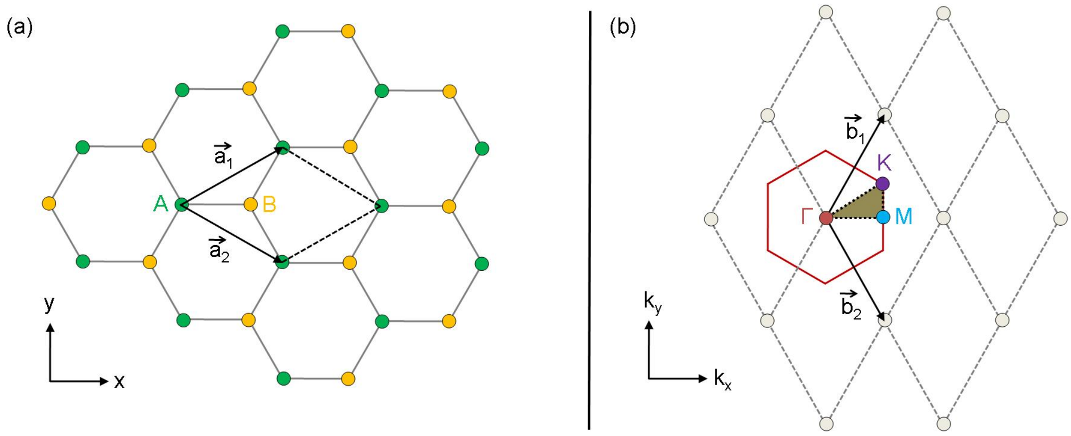

Figure 1: In (a) the lattice structure of graphene is presented. The unit vectors $\vec{a_1}$ and $\vec{a_2}$ define the unit cell, consisting of two inequivalent points A and B. In (b) the reciprocal lattice, presented by the dashed lines, is formed by the reciprocal lattice vectors $\vec{b_1}$ and $\vec{b_2}$. The honeycomb is the first Brillouin zone with the high symmetry points Γ, K and M.

The given Brillouin zone, which is the Wigner-Seitz cell of the reciprocal lattice, can now be calculated with the defining condition between a unit vector $\vec{a_i}$ in real and $\vec{b_j}$ in reciprocal lattice, $\vec{a_i} \cdot \vec{b_j} = 2\pi\delta_{ij}$, with the Kronecker δ. This gives the values for the reciprocal unit vectors

$$\vec{b_1} = \left(\frac{2\pi}{\sqrt{3}a}, \frac{2\pi}{a}\right), \quad \vec{b_2} = \left(\frac{2\pi}{\sqrt{3}a}, -\frac{2\pi}{a}\right). \tag{3}$$

Starting to build the reciprocal lattice, shown in figure 1 (b), at the Γ-point ($\vec{\Gamma} = (0,0)$), the Brillouin zone turns out to have a honeycomb structure with two other important points called K and M, with $\vec{K} = (2\pi/\sqrt{3}a, 2\pi/3a)$ and $\vec{M} = (2\pi/\sqrt{3}a, 0)$, located at the corner and the center of the edge, respectively. These points are giving the highest symmetry of the Brillouin zone. Later we have to consider, that not all K points have to be treated equally, and therefore to distinguish between two different types. But first the dispersion relation $E(\vec{k})$ for this triangle ΓKM will be calculated in order to find out the electron behavior in this area.

2.2 The band structure

While the σ-bands are strongly determining the lattice structure of graphene, mainly the π-bands are responsible for its electronic properties, since band structure calculation shows, that the σ-bands are far away from the Fermi energy[12]. To calculate the dispersion relation for the π-bands, we can use the tight binding theory and we take into account only nearest neighbor interactions. In this approximation, where we use a linear combination of the tight binding Bloch functions to express the eigenfunctions in graphene, the dispersion relation $E_g(\vec{k})$[12] of the bonding(+) π-band and anti-bonding(−) π^*-band of a graphene monolayer, shown in figure 2, is given by

$$E_g(\vec{k}) = \pm\gamma_0 \cdot \sqrt{|f(\vec{k})|^2} = \pm\gamma_0 \cdot \left\{1 + 4cos\left(\frac{\sqrt{3}k_x a}{2}\right) cos\left(\frac{k_y a}{2}\right) + 4cos^2\left(\frac{k_y a}{2}\right)\right\}^{1/2}. \tag{4}$$

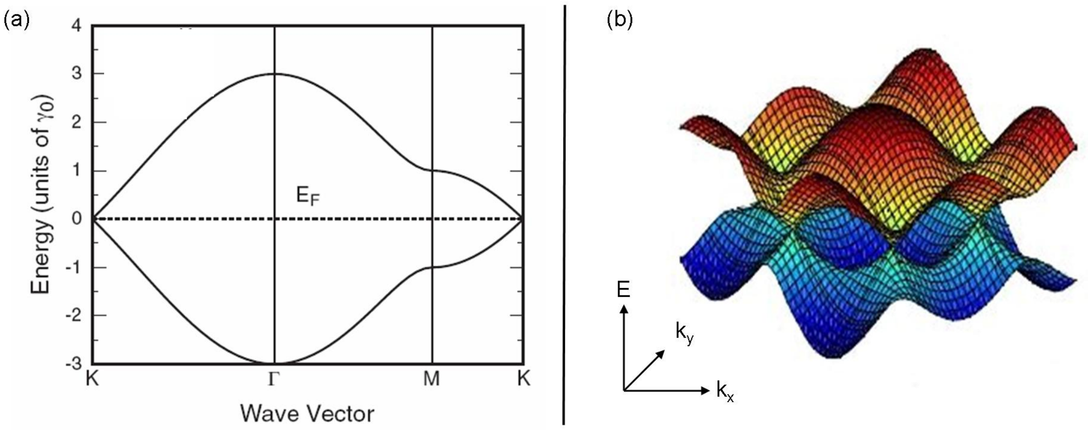

Figure 2: In (a) the dispersion relation for the π-bands is presented along the triangle of the high symmetry points, from $K \to \Gamma \to M \to K$. (b) gives a three-dimensional impression of the dispersion relation.

Since both π-bands, also known as valence and conduction band, can be occupied by two electrons with either spin up or spin down and there are two electrons per unit cell, the lower anti-bonding π^*-band is fully occupied and the Fermi energy is equal zero. At a finite temperature or due to radiation with light, an electron-hole pair can be excited, what means creating two nearly free charge carriers in the conduction band and the valence band, respectively, which are following the dispersion, given in equation (4). The energy values for the high symmetry points are $E(\vec{\Gamma}) = \pm 3\gamma_0$, $E(\vec{M}) = \pm\gamma_0$ and $E(\vec{K}) = 0$. The latter case makes graphene to zero bandgap semiconductor. Now it is interesting to look at the behavior of the dispersion relation at the K point. For the Taylor expansion around K we get $|f(\vec{k})|^2 = (3a^2/4)|\vec{k} - \vec{K}|^2 + O(|\vec{k} - \vec{K}|^3)$, since the constant term, the two first and the mixed derivatives vanish. This leads with equation (6) to the following approximation for the dispersion relation around the K point

$$E_g(\vec{k} + \vec{K}) = \varepsilon(\vec{k}) = \pm\frac{\sqrt{3}}{2}\gamma_0 a|\vec{k}|, \tag{5}$$

which is linear in $|\vec{k}|$. As a result we can write the dispersion relation for the charge carriers in the vicinity of K in a usual way as $\varepsilon(\vec{p}) = \pm\tilde{c} \cdot |\vec{p}|$, with the momentum $\vec{p}$ and the so-called Fermi velocity $\tilde{c}$, which can be calculated after equation (5) and $\vec{p} = \hbar\vec{k}$, to

$$\tilde{c} = \frac{\sqrt{3}\gamma_0 a}{2\hbar} \approx 10^6\,\frac{\mathrm{m}}{\mathrm{s}}. \tag{6}$$

Due to this behavior, the charge carriers can be treated with the Dirac equation. This results in a spinor structure for the eigenfunctions, considering not only the two inequivalent points A and B but also a distinction between to kinds of K points, called K and K', located alternately at the corners of the Brillouin zone. In the effective-mass description, the resulting four-dimensional eigenfunction $\vec{\psi}(\vec{r})$ and the corresponding Hamiltonian H_0 are giving the equation for the eigenvalues, that can be written as two Dirac equations, for K and K', of the form

$$\gamma(\vec{k} \cdot \vec{\sigma})\vec{\psi}_K(\vec{r}) = \epsilon\vec{\psi}_K(\vec{r})^{[2]}, \tag{7}$$

where $\gamma = (\sqrt{3}/2)a\gamma_0$, $\vec{k}$ is the momentum operator and $\vec{\sigma} = (\sigma_x, \sigma_y)$ the Pauli spin matrix vector. The eigenvalues of these equations, given by cones shown in figure 3 (a), for the so-called Dirac points K and K' can be calculated to

$$\varepsilon_s(\vec{k}) = s\gamma|\vec{k}|^{[2]}, \tag{8}$$

with $s = +1$ for the conduction band and $s = -1$ for the valence band which is consistent with equation (5). With this, the density of states $D(\varepsilon)$, shown in figure 3 (b), is given by

$$D(\varepsilon) = \frac{|\varepsilon|}{2\pi\gamma^2} = \frac{|\varepsilon|}{2\pi(\tilde{c}\hbar)^2}^{[2]}. \tag{9}$$

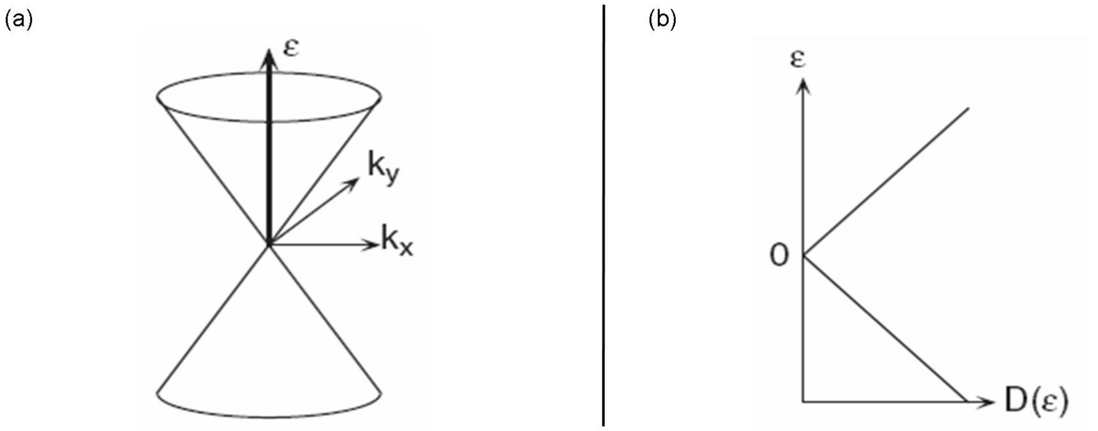

Figure 3: In (a) the energy bands according to equation (7) are shown, given by cones at the points K and K'. In (b) the density of states $D(\varepsilon)$ is presented, linear in the energy and vanishing at $\varepsilon = 0$.

2.3 Magnetic properties

In the presence of a magnetic field perpendicular to the graphene layer, with $\vec{B} = B \cdot \vec{e}_z = (\partial A_y/\partial x) - (\partial A_x/\partial y)$, a possible vector potential is $\vec{A} = Bx \cdot \vec{e}_y$. The momentum vector in a magnetic field is therefore given by $\vec{k} = -i(\partial_x, \partial_y) + (e/\hbar)(0, Bx)$, with the elementary charge e. Additionally, we can note $[k_x, k_y] = -(i/l^2)$ with the magnetic length $l = \sqrt{\hbar/eB}$. Defining the operators $a = (l/\sqrt{2})(k_x - ik_y)$ and $a^\dagger = (l/\sqrt{2})(k_x + ik_y)$, with $\left[a, a^\dagger\right] = 1$, and neglecting the spin splitting energy, the Hamiltonian H_0 for one K point can be written as

$$H_0 = \frac{\sqrt{2}\gamma}{l}\begin{pmatrix} 0 & a \\ a^\dagger & 0 \end{pmatrix}. \tag{10}$$

If we further define a function $h_n(x, y) = ((a^\dagger)^n/\sqrt{n!})h_0(x, y)$, with $ah_0(x, y) = 0$, we can note $a^\dagger h_n = \sqrt{n+1}h_{n+1}$ and $ah_{n+1} = \sqrt{n+1}h_n$. Now we can write the eigenfunctions of the Hamiltonian H_0 in a magnetic field as

$$\psi_n = \frac{1}{\sqrt{2}}\begin{pmatrix} \text{sgn}(n)h_{|n|-1} \\ h_{|n|} \end{pmatrix}^{[2]}, \tag{11}$$

with $n = \pm1, \pm2, ...$ and the signum function sgn(x) $= +1$ for $x > 0$ and sgn(x) $= -1$ for $x < 0$. The corresponding eigenvalues or so-called Landau levels are given by

$$\varepsilon_n = \text{sgn}(n)\frac{\sqrt{2}\gamma}{l}\sqrt{|n|} = \text{sgn}(n)\tilde{c}\sqrt{2\hbar eB|n|} = \text{sgn}(n)\epsilon_0\sqrt{|n|}^{[2]}, \quad n = \pm1, \pm2, ..., \tag{12}$$

which will in the following also be denoted by L_n and are shown in figure 4. The square root dependence on the magnetic field has to be pointed out here, since this is a special behavior, which is in contrast to a standard two-dimensional electron gas with a linear dependence in B. Additionally, a Landau level at $\varepsilon = 0$ occurs with the eigenfunction $\psi_0 = (0, h_0)$. As a result, charge carriers in a magnetic field can only have discrete energy values given by equation (12) and $\varepsilon = 0$. The quantization of a two-dimensional electron gas of the size L_x, L_y in a magnetic field shows, that the degeneracy ρ of the Landau levels, is constant with $\rho = (L_x L_y eB/2\pi\hbar)^{[3]}$. The energy values E_s, where the distribution switches to the next level, is given by $E_s = \pm\epsilon_0\sqrt{s + 1/2}^{[9]}$, with $s = 0, 1, 2....$

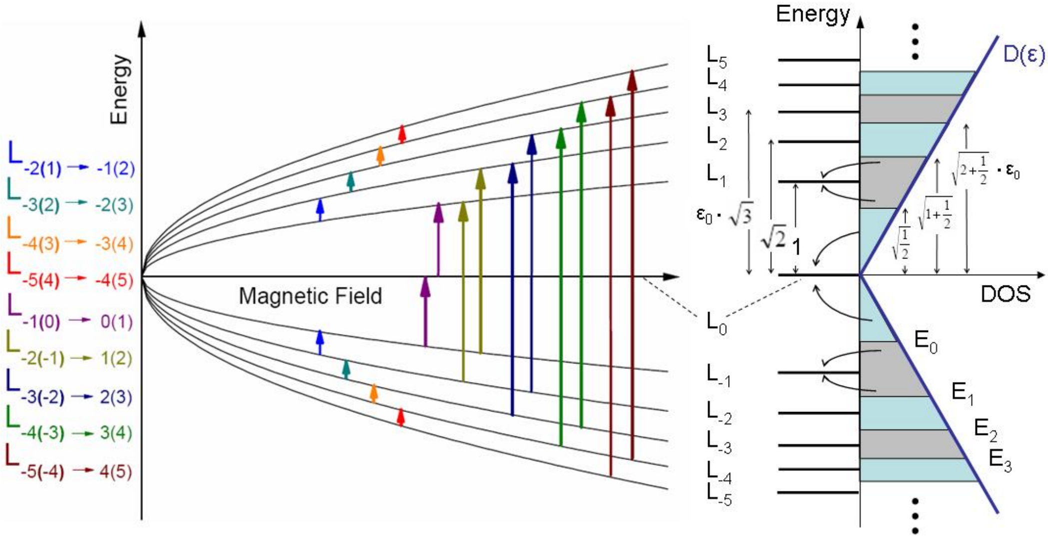

Figure 4: The right side shows, how the number of charge carriers, given by the density of states $D(\varepsilon)$, is distributed to the Landau levels L_n. The left presents Landau levels according to equation (12) and the dipole-allowed transitions $L_{n\rightarrow|n|\pm1}$ between them. Transitions are marked in the same color, because we generally can not distinguish between them in transmission measurements, since they show the same energy difference.

If we assume a given Fermi energy ε_F, which means an occupation of the Landau levels up to a certain energy with charge carriers, a transition of charge carriers between to levels is only possible, if the initial level is occupied and the final one is not full. In addition, we have to consider the probability of a certain transition, given by the corresponding dipole matrix element of the two states. The resulting selection rules, which define the dipole-allowed transitions from a level L_n to L_m, presented in figure 4, are given by $|n| = |m| \pm 1$[11]. Another important and helpful value is the filling factor ν, defined by the number of charge carriers N divided by the degeneracy ρ, and therefore specifies the number of occupied Landau levels. Considering the spin degeneracy it holds

$$\nu = \frac{N}{2\rho} = \frac{N}{L_x L_y} \cdot \frac{\pi\hbar}{eB} = n_c \cdot \frac{\Phi_0}{B}, \tag{13}$$

where N is the number of charge carriers, either holes or electrons, depending on the doping of the sample, $n_c = N/A$ is the carrier density and $\Phi_0 = h/2e$ the quantum flux. The filling factor is defined for either holes or electrons and for one spin and one K point. This means, that every Landau level is additionally degenerated four times. However, since the level at $\varepsilon = 0$ can be populated by electrons and holes, they have to share this degeneracy and when we talk about one type of charge carriers the level L_0 is degenerated two times. At e.g. a filling factor $\nu = 2$, the first Landau level is fully occupied, at $\nu = 6$ the second and so on.

2.4 Epitaxial graphene

Graphene layers have been among us for a very long time, since they are building, stacked once upon the other, graphite. Even though, until the beginning of this century, it was not possible to extract single or several of them, in a way to do reasonable experiments. In principle there are two ways to produce graphene. One is to exfoliate graphene layers from graphite by simply putting a tape on it, pressing and peeling it away. The advantage of this procedure is the possibility to isolate single or very few layers, which usually are showing the typical ABAB stacking of graphite. Another way is to grow graphene epitaxially (figure 5) on certain surfaces, e.g. silicon carbide. By heating SiC, silicon desorbs first from the surface and a few layers of graphene on the top of the substrate are generated, where it should be mentioned, that the first layer on top of the SiC surface is strongly bonded and shows now graphene like behavior[5]. The number of layers can be manipulated by varying the period or the temperature of heating. Since the work function in SiC is higher than in graphene, the chemical potential of the whole sample is above the Dirac point, and therefore the graphene layers are n-doped, at a level decreasing with the distance to the substrate[5]. In addition, the layers are not grown homogeneously on the surface, what leads to regions with a different number of layers. Even though there are interactions between the layers, which are leading e.g. in a bilayer to a nonlinearity of the dispersion relation at the Dirac point[1], the electrons in epitaxial graphene are showing the Dirac like behavior at the points K and K'.

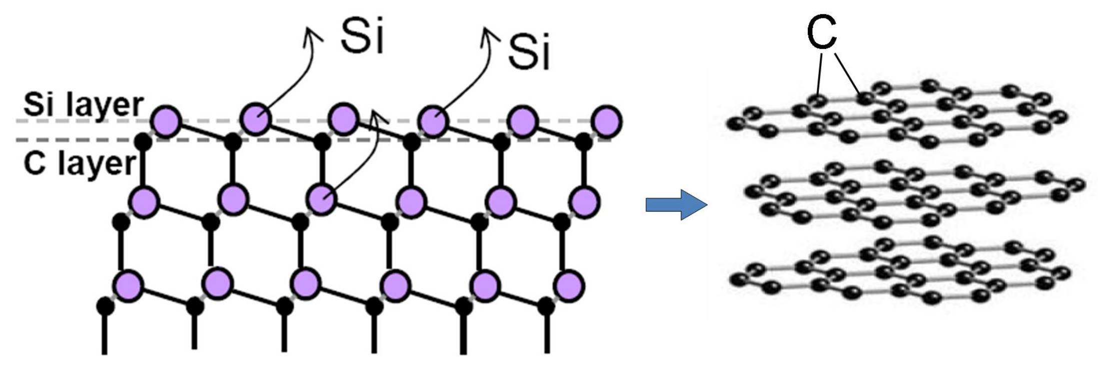

Figure 5: The process of epitaxial growth of graphene on SiC is presented. Through the evaporation of silicon atoms at the surface, several layers of graphene are created, bonded on the top of the substrate.

3 Experimental setup

In this section the main experimental setup will be discussed. After an introduction to the spectrometer, that was used for infrared measurements, the magnets will be presented. In the end a scheme of the alignment and the measurement is given.

3.1 The spectrometer

The type of spectroscopy, that is used for the experiments, is based on the principle of an Michelson interferometer. The light beam of a polychromatic light source is guided through a beam splitter where the light is reflected and transmitted, respectively. Each of the two different beams is again reflected at a mirror and recombined, whereas one of the mirrors can be moved parallel to the beam direction. Depending on the difference between the path length of the two beams, which can be adjusted by moving the mirror, the wavelengths of the light source are interfering in a constructive or destructive way after they recombined. If we denote the distance of the movable mirror from the position, where the two path lengths are equal, with x, the total optical displacement becomes $2x$ and the conditions for total constructive or destructive interference are $2x = n\lambda$ and $2x = (n + 1/2)\lambda$ with $n = 0, 1, 2, \dots$. By measuring the intensity of the two combined beams as a function of the position x of the mirror, an interferogram can be recorded. It directly reflects the conditions given above, since it shows, if only one wavelength is being considered, a periodic shape of maxima and minima in the intensity. The interferogram of the whole spectrum, shown in figure 6, just consists of the superposition of the interferograms of the single wavelengths in the spectrum. It has its maximum in intensity at $x = 0$, since there the optical displacement is zero for all wavelengths, and decreases in the positive as well as in the negative x direction. The formalism of Fourier transformation allows us to calculate the spectrum from the interferogram and the other way around. Since the recorded interferogram $I(n \cdot \Delta x)$ is no continuous function, but consists of certain points N equally spaced by the distance Δx, the discrete Fourier transformation hast to be used to calculate the spectrum

$$S(k \cdot \Delta\omega) = \sum_{n=0}^{N-1} I(n \cdot \Delta x) \exp\left(\frac{i2\pi kn}{N}\right). \tag{14}$$

In turn the spectrum $S(k \cdot \Delta\omega)$ consists of spectral points k equally spaced by $\Delta\omega$, witch denotes the resolution. It is inversely correlated to the spacing Δx with $\Delta\omega = (N\Delta x)^{-1}$.

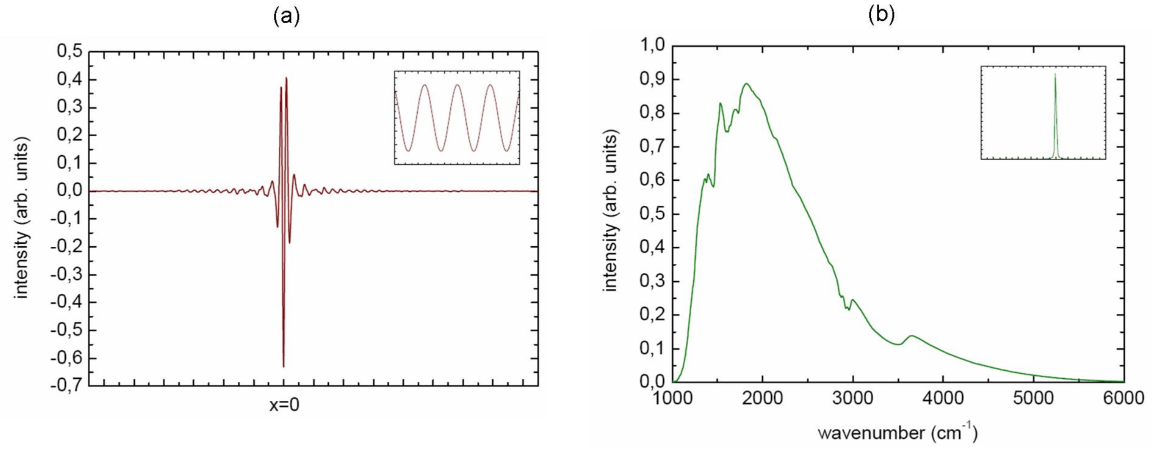

Figure 6: (a) shows the interferogram and (b) the corresponding spectrum of a globar light source and a CaF_2 beam splitter, recorded by the spectrometer IFS 113v of the firm BRUKER© and detected by a bolometer with a silicon window. The insets show the corresponding figures for a single wavelength with a finite line width.

The great advantage of this procedure is, that the system, which detects the light beam need not to be wavelength sensitive, even though the whole spectrum is detected at once, by means of moving the mirror a certain distance. This allows to measure the transmittance of a sample over a wide frequency range within a few seconds. For the main experiments the spectrometer IFS 113v of the firm BRUKER$^{©}$ was used, which has three light sources for the infrared region. For the far infrared (FIR) a high pressure mercury vapor lamp recommended for $k = 10 - 700\text{cm}^{-1}$, for the middle infrared (MIR) a silicon carbide stick at 1500°C, called globar ($100 - 3000\text{cm}^{-1}$), and a tungsten halogen lamp ($2000 - 10000\text{cm}^{-1}$) for the near infrared (NIR). Additionally, there are certain beam splitters, that can be used for the desired spectral region. For the FIR and MIR there are three dielectric Mylar foils of the thickness 6, 12 and 23 μm (M6, M12, M23), whose maximum intensity is, with increasing thickness, shifted to lower wave numbers. For the MIR and FIR we can use a Ge coated KBr or a Si coated CaF_2 crystal. The construction and the path rays are shown in figure 7. An extension to a Michelson interferometer occurs, since the split beams are reflected on the different sides of one movable mirror, which will be referred to as the scanner. This just indicates an optical displacement of $4x$, but has the advantage, that the total path length $N \cdot \Delta x$ is increased, what results in a higher resolution. In addition, a certain resolution can be set by changing the spacing Δx, but it has to be taken into account, that a too low resolution is causing interference effects on the sample and setting it too high can annihilate information from the spectrum. Further possibilities are putting wavelength filters in the beam path to cut the spectrum or setting a certain aperture, which limits the diameter of the light beam. Additionally, the whole spectrometer is under vacuum to avoid the absorption of light by water vapor.

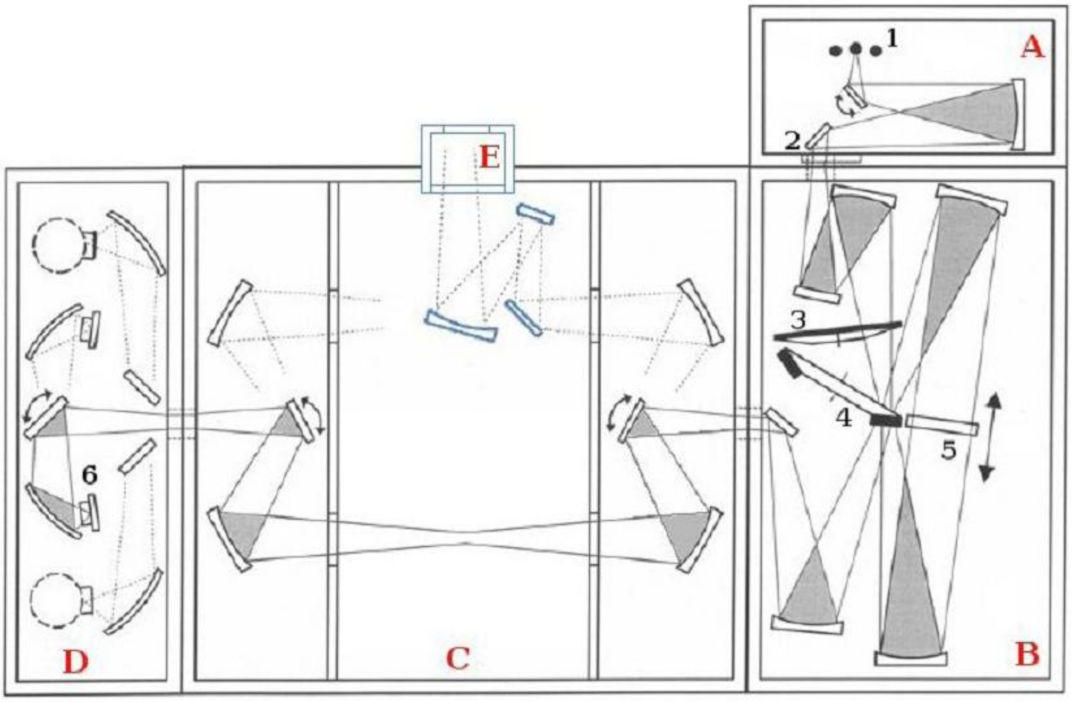

Figure 7: The setup of the IFS 113v spectrometer of the firm BRUKER$^{©}$. In chamber A the beam of the light source (1) is guided through the aperture (2) entering the chamber B. Here it passes the optical filters (3) and runs through the interferometer, which consists of the beam splitter (4) and the scanner (5). In the next chamber the beam can either be send to an external sample and detection system E or guided in the internal sample chamber C. There it runs through the sample and is directed to the chamber D with the internal detector (6).

3.2 The magnets

Measurements have been performed in two different magnets. A superconducting coil and a resistive magnet. The superconducting coil, which provides a very good field homogeneity, is located in a cryostat filled with liquid helium and runs therefore under a temperature of either 4K (B $\leq$ 11) or additionally, by pumping the helium bath, at 2K, where 13T can be reached. The resistive magnet is presented in figure 8. It is supplied by a total power of 24MW, reaches continuous fields up to 34T and has a homogeneity of $700 \cdot 10^{-6} \Delta B \cdot (B \cdot \mathrm{cm})^{-1}$. The current under the maximum field equals 30000A, what requires an appropriate cooling system dissipating the generated heat. The maximum field is limited by the mechanic resistance of the coils, since the Lorentz force $\vec{F} = \vec{j} \times \vec{B}$ leads the magnet to expand in the radial direction, as well as by the possibility to keep the coil below a temperature of 100°C to prevent the creation of steam, which is not appropriate to cool the system. Thus the material, that is used for the coil, consisting mostly of copper, has to be optimized in mechanical strength, whereas the electrical resistance has to be minimized.

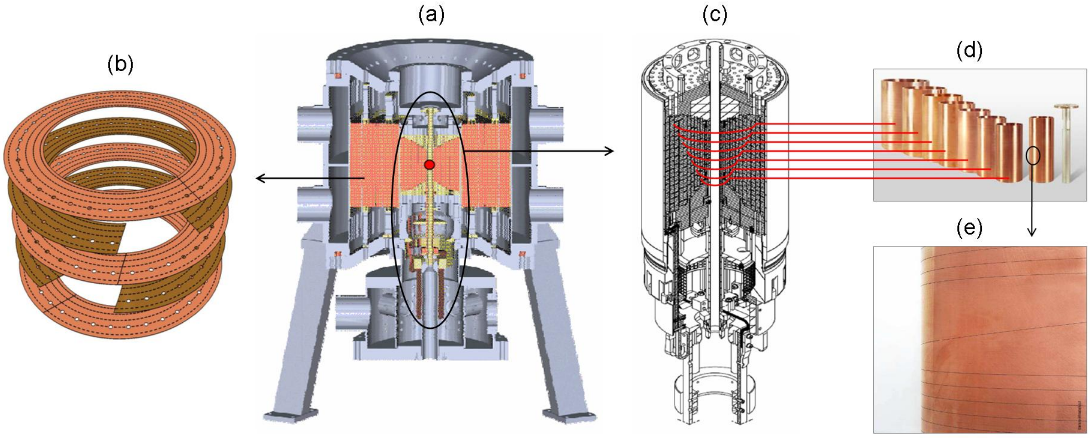

Figure 8: (a) shows the resistive magnet M9. Its outer part is a bitter coil (b), which consists of single discs stacked upon each other. The isolation between them is interrupted a few centimeters every 45 degrees with respect to each other, what allows the current to flow from disc to disc. The demineralized cooling water is running through the holes, whose density has to increase towards the center, as well as the current density does. The inner part (c) consists of several coils (d) which are fit into each other with space between for the water cooling. The single coils are barrels with a thickness in the range of 1cm and have a horizontal isolation in the form of a helix structure (e). The inner, empty core, has a diameter of 34mm and can be filled by liquid helium, what provides experiments not only on high fields but also at low temperatures.

3.3 Basic measurement and beam alignment

The main part of the experiments was to measure the relative transmission $T_{rel}(k, B)$ of samples, with a two-dimensional electron gas, in the infrared region and at low temperatures, performed in a magnetic field B. The modulated light beam, produced by the spectrometer, is running through the sample and detected by a bolometer. This consists of a doped silicon device, which is connected to an electric circuit. If it is hit by light, its temperature increases and its resistance is reduced. By measuring the voltage U on the bolometer, the change ΔU can directly be correlated to the intensity of incoming light. After detection, the signal is amplified and guided back to the spectrometer. This is directly connected to a computer, where the corresponding spectrum can be calculated. The full beam alignment, when the magnetic field is perpendicular to the sample layer, is shown in figure 9. By dividing the spectrum at a certain magnetic field by the one at $B = 0$T, we clear out the influence of every component in the beam path, whose transmittance is not changing with magnetic field, as it is the beam splitter, optical filters, windows and a substrate the sample is possibly grown on. However the sensitivity of the bolometer is a polynomial function of the magnetic field. This can be neglected for low fields (0T < B < 1T), and thus the relative transmission $T^{l}_{rel}(k, B)$ for this low region is just calculated by the division of the two spectra S with

$$T^l_{rel}(k,B) = \frac{S(k,B)}{S(k,B=0)}. \tag{15}$$

To get rid of the magnetic field sensitivity of the bolometer for higher fields, we have to make a reference spectrum $S_{ref}(k,B)$ and $S_{ref}(k,B=0)$, which consists of the transmission of either a hole or a material, that is not sensitive with magnetic field. By dividing the spectra S of the sample by their corresponding reference S_{ref}, we take into account the sensitivity of the bolometer and the relative transmission at high fields is given by

$$T^h_{rel}(k,B) = \frac{S(k,B)/S_{ref}(k,B)}{S(k,B=0)/S_{ref}(k,B=0)}. \tag{16}$$

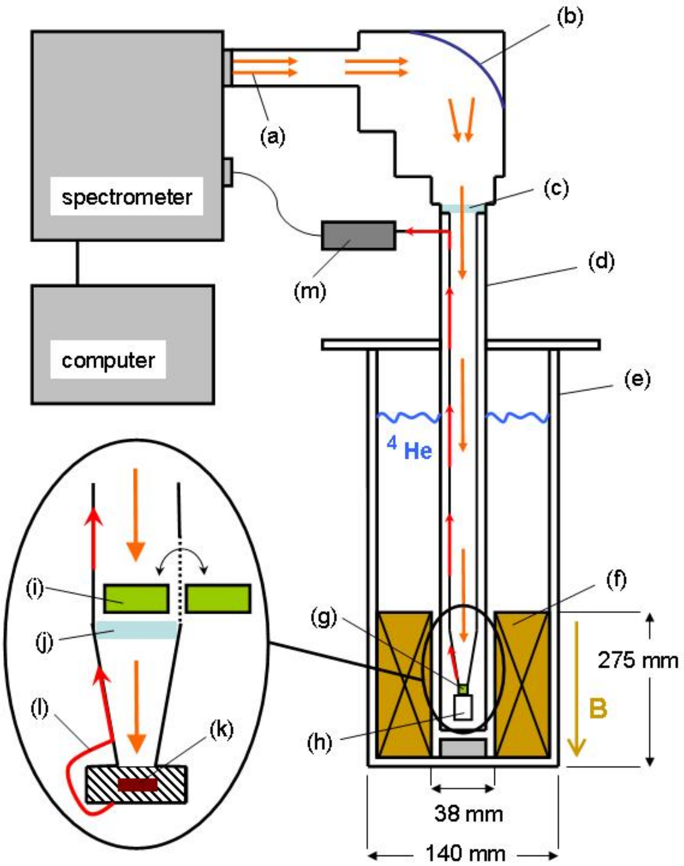

Figure 9: After the light beam (a) runs through the spectrometer it is focused with a parabolic mirror (b) and then guided through a window (c) into the probe (d). The window is part of the probe and can be substituted. The probe is placed in a cryostat (e), which is filled with liquid helium. This not only provides the required temperature for the superconducting coil (f), which is located at the bottom of the cryostat, but also a cooling down of the inner part of the probe, that is first pumped to remove air and water vapor and then filled by helium gas to provide the thermal contact. After the light beam passes the sample system (g), it is detected by the bolometer (h). The sample and detection system are shown in the enlargement. In the sample system one can switch between two positions (i) two make a reference measurement under the same circumstances. After passing sample or reference the light beam runs through the window (j) of the bolometer and is detected by the semiconductor device (k). Then it is relayed by a wire (l) out of the cryostat to a preamplifier (m) and from this back to the spectrometer and the computer, where the spectrum is calculated.

4 Experiments

The following section presents the experiments, which were done in three main parts, and an analysis of the data. After an introduction of the epitaxial graphene samples, the first infrared transmission measurements, that have been performed in magnetic fields, will be shown and discussed. Since the results were promising, but could partly not be explained with a regular model, the samples have been exfoliated to investigate the extracted parts. In addition Raman studies have been performed on the exfoliated and remaining parts of the samples, to verify the presence of graphene. In the end, the new samples have again been studied, concerning their transmission in the infrared region with the presence of a magnetic field.

4.1 The samples

Three different samples 7M8, 837 and 838, with a few graphene layers grown epitaxially on the C face of 4H-SiC, have been investigated in this study. All samples have been produced by the group of Walter A. de Heer under the supervision of Claire Berger (School of Physics, Georgia Institute of Technology, Atlanta, GA 30332, USA). The latter two samples were produced in the same series.

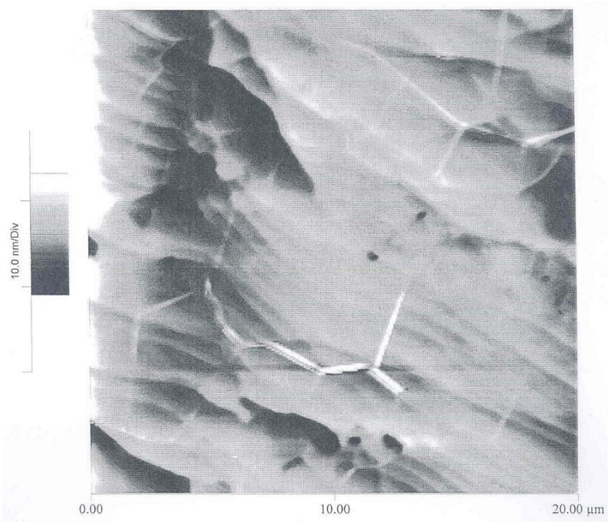

Figure 10: An image of the sample 7M8 is shown, made by scanning tunneling microscopy. An indication of the hexagonal structure can be seen.

4.2 Infrared transmission studies

Even if we do not know the exact number of graphene layers, we can be sure that they have a decreasing carrier density with an increasing distance to the substrate, due to successive screening effects. Since this leads to different filling factors, we can, in the presence of a magnetic field, expect Landau level transitions corresponding to different Fermi energies. For simplicity we will denote certain transitions as follows:

$$\begin{aligned}
\alpha &: L_{-1(0)\to 0(1)} \\
\beta &: L_{-2(-1)\to 1(2)} \\
\chi &: L_{-3(-2)\to 2(3)} \\
\delta &: L_{-4(-3)\to 3(4)} \\
\eta &: L_{-5(-4)\to 4(5)} \\
\kappa &: L_{-2(1)\to -1(2)}
\end{aligned}$$

First it has to be mentioned, that silicon carbide has two bands of total absorption between 700cm^{-1} and 1400cm^{-1}, and between 1500cm^{-1} and 1750cm^{-1}, what narrows the measurable spectral region to 50-700cm^{-1} and 1750-8000cm^{-1}. The limit in the far and near infrared region is dependent on the light source and the signal to noise ratio. The first transmission measurements have been performed on the sample 7M8, using the superconducting coil at a temperature of 2K. Beside the globar light source (MIR), we used for the low spectral region up to 400cm^{-1} the beam splitter M6, that has its maximum in transmission between 200cm^{-1} and 300cm^{-1}, and a bolometer with a polyethylene window, which has a transmission larger than 50% up to 450cm^{-1}. For the high spectral region, after the absorption band, we used the CaF$_2$ beam splitter, with a transmission of 90% between 700cm^{-1} and 10000cm^{-1}, a bolometer with a silicon window, that shows, reduced by some phonon frequencies, a transmission of 50% at wave numbers higher than 600cm^{-1} and a hole as reference. Spectra with magnetic fields at 0.2T-1T and 4T-10T are shown in figure 11. We can clearly see the absorption lines as a decrease in intensity of the transmission at energies $\Delta\varepsilon_{n,|n|\pm 1} = \varepsilon_{|n|\pm 1} - \varepsilon_n$ due to charge carrier transitions from Landau level L_n to $L_{|n|\pm 1}$. The broadening of the lines occurs due to interactions with defects. We can also see, that the intensity of the absorption lines increases with the magnetic field, which is in contrast to a standard two-dimensional electron gas with parabolic dispersion relation, where the intensity remains constant. In the low field region we see the transition α, which can be followed down to 0.2T. Since we know the sample is n-doped due to the epitaxial growth, the intra band transition κ, which can be seen down to 0.7T, is electron like. For the high field region we can see the transitions β, χ, δ and η, due to the creation of an electron hole pair. They exhibit a line splitting, what we will be specified from now on with an index 1 and 2 for the left and the right peak, respectively. This splitting was not expected and is uncommon for epitaxial graphene up to now. The transitions $\beta_{1,2}$ can be followed clearly down to 6T and the remaining ones down to 4T, where the splitting still remains but is very hard to see due to the decrease of intensity. Of course there occur also higher transitions. However, they will not be denoted here, since they could not be located definitely.

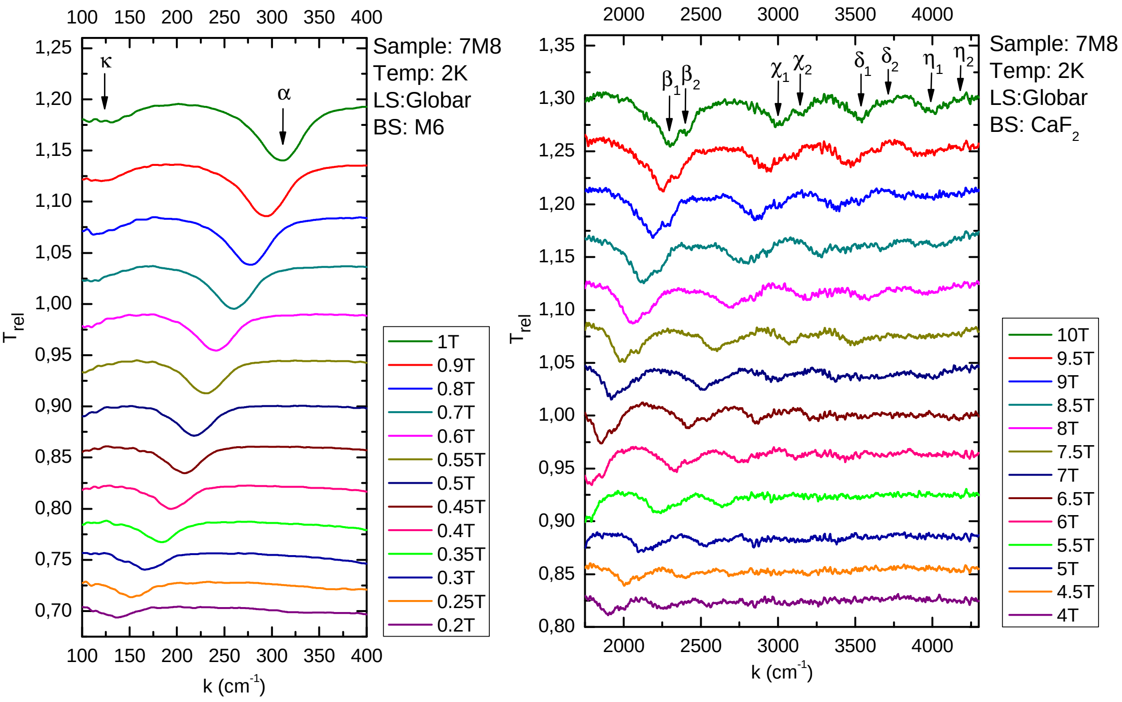

Figure 11: Relative transmission $T_{rel}(w, B)$ of the sample 7M8. Taken with a globar light source and two different beam splitters at various magnetic fields. The spectra are smoothed with an adjacent averaging.

To verify the Dirac like behavior of the charge carriers, we can plot the energy $\Delta\varepsilon_{n,|n|\pm1}$ as a function $\sqrt{B}$, where we should find, according to equation (12), a linear dependence, since

$$\Delta\varepsilon_{n,|n|\pm1} = \left(\mathrm{sgn}(|n|\pm1)\sqrt{|n|\pm1} - \mathrm{sgn}(n)\sqrt{n}\right)\tilde{c}\sqrt{2\hbar e}\cdot\sqrt{B}, \quad n = 0, \pm1, \pm2, ..., \tag{17}$$

whereas the sgn-function only occurs for $|n| > 0$. The plot for the transitions α, β, $\beta_{1,2}$, $\chi_{1,2}$, $\delta_{1,2}$, and $\eta_{1,2}$ is shown in figure 12. The linear dependence can be seen clearly and verifies therefore the existence of ultra relativistic charge carriers in the vicinity of the Dirac points in epitaxial graphene. With a linear fit of the data we calculated, according to equation (17), the Fermi velocity $\tilde{c}$ of the sample 7M8 for the different transitions. The values are presented in table 1. Looking at this data it seems, that the value for $\tilde{c}$ is not dependent on a certain transition, but on the splitting of itself. This can be due to graphene flakes on the substrate, which show different Fermi velocities, as well as different interactions between the layers. The values for α and β are different, since the splitting in this magnetic field region is small compared to the width of the absorption peak. As a result only one peak can be seen, which gives a mean value for $\tilde{c}$. The values of the left peak are in very good agreement to other studies on epitaxial graphene[10].

	α	β	β_1	β_2	χ_1	χ_2	δ_1	δ_2	η_1	η_2
$\tilde{c}$ [10^6m/s]	1.05	1.06	1.03	1.07	1.03	1.08	1.03	1.08	1.03	1.08

Table 1: The Fermi velocity $\tilde{c}$ derived from individual transitions is presented. The values are observed from the sample 7M8. The uncertainty is 2% ($0.02 \cdot 10^6$m/s).

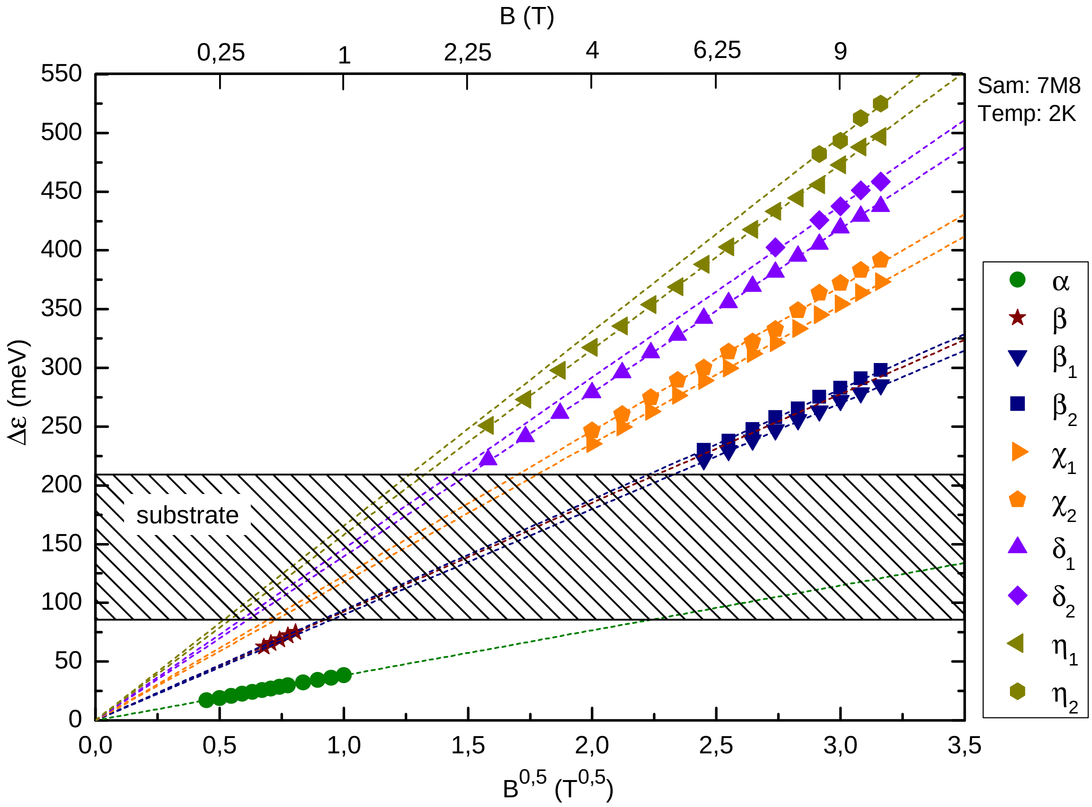

Figure 12: We can see the energies $\Delta\varepsilon$ of various transitions as a function of $\sqrt{B}$ for the sample 7M8. The dotted lines are linear fits, giving the values for the Fermi velocity $\tilde{c}$.

The samples 837 and 838 have been investigated in a similar way. We used the globar, a silicon window bolometer, silicon as reference and worked at a temperature of 4K. For the spectral region between 125cm^{-1} and 500cm^{-1} we used the beam splitter M6 and between 1750cm^{-1} and 4000cm^{-1} CaF$_2$. Additionally, we studied the spectral region between 400cm^{-1} and 700cm^{-1}, to see how the splitting evolves. Here we used the the KBr beam splitter. Spectra of the sample 837 with magnetic fields 0.3T-4.5T and 5T-11T are shown in figure 13. The results for the low and high field region are comparable to the sample 7M8, whereas now the noise for the low spectral region is higher, and for high frequencies lower. The increase in the noise is due to the use of the silicon window bolometer instead of the one with a polyethylene window, which has a higher transmittance in this region. The decrease of the noise for the high spectral region is caused by truncating the interferogram to remove interference effects on the sample, what has not been done for 7M8. At B=2T we can clearly see the development of the splitting for the transition α, that can be followed to higher fields. The transitions $\beta_{1,2}$ can be followed down to 6.5T and the transitions $\chi_{1,2}$ can be seen clearly down to 5T. The spectra of the sample 838 are similar, except of the fact, that the splitting could not be identified before the absorption band definitely. The plot for the transition energies $\Delta\varepsilon_{n,|n|\pm 1}$ as a function of $\sqrt{B}$ for 837 is shown in figure 14. The values for the Fermi velocity, presented in table 2, are similar to the ones we obtained for 7M8.

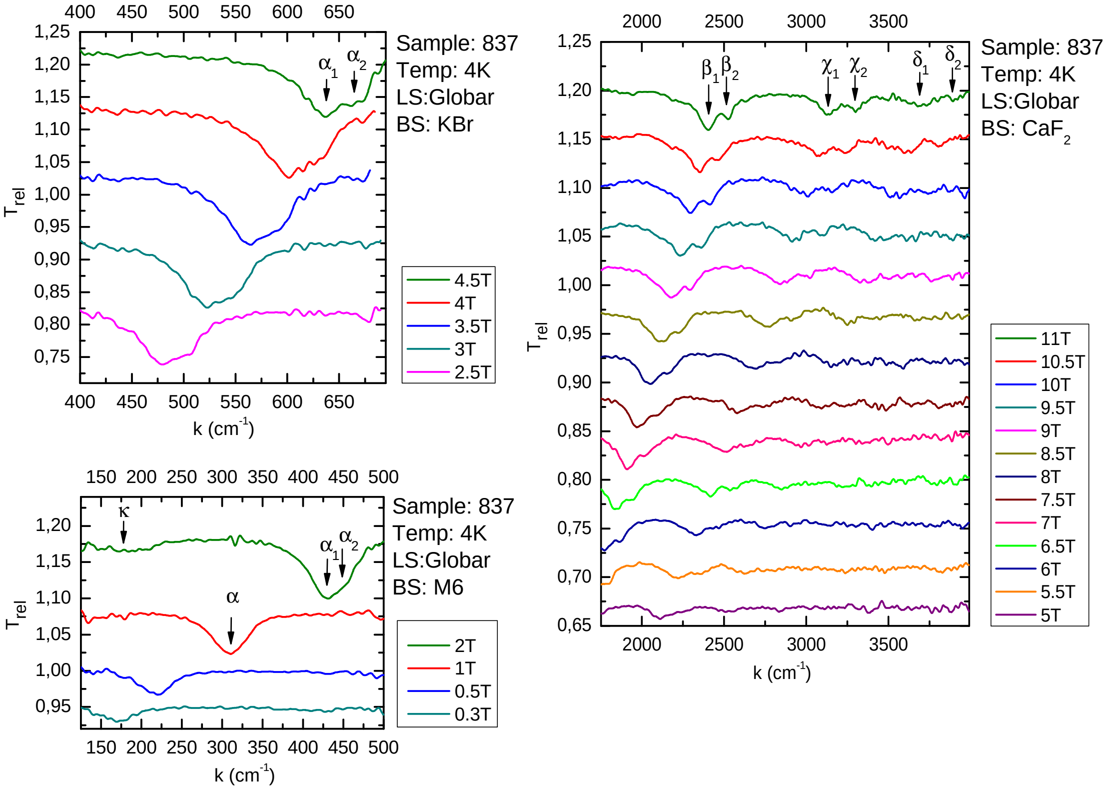

Figure 13: Relative transmission $T_{rel}(w, B)$ of the sample 837. Taken with a globar light source and three different beam splitters at various magnetic fields. The spectra are smoothed with an adjacent averaging.

	α	α_1	α_2	β_1	β_2	χ_1	χ_2	δ_1	δ_2
$\tilde{c}$ (10^6m/s), 837	1.05	1.02	1.08	1.03	1.08	1.03	1.09	1.02	1.08
$\tilde{c}$ (10^6m/s), 838	1.05	-	-	1.03	1.08	1.03	1.09	1.03	1.08

Table 2: The Fermi velocity $\tilde{c}$ derived from individual transitions is presented, with an uncertainty of 2%.

Concerning the appearance of certain transitions, we can make some considerations about the filling factors of the different layers. Since we see the transition κ, there is at least one graphene layer, where the Landau level L_1 is populated and the level L_2 is not full. This implies that the filling factor ν of this layer at the given magnetic field is $2 < \nu < 10$. For the higher transitions we can expect at least one layer with a filling factor $\nu < 6$. To investigate more the properties of the layers, we started to exfoliate the sample 837.

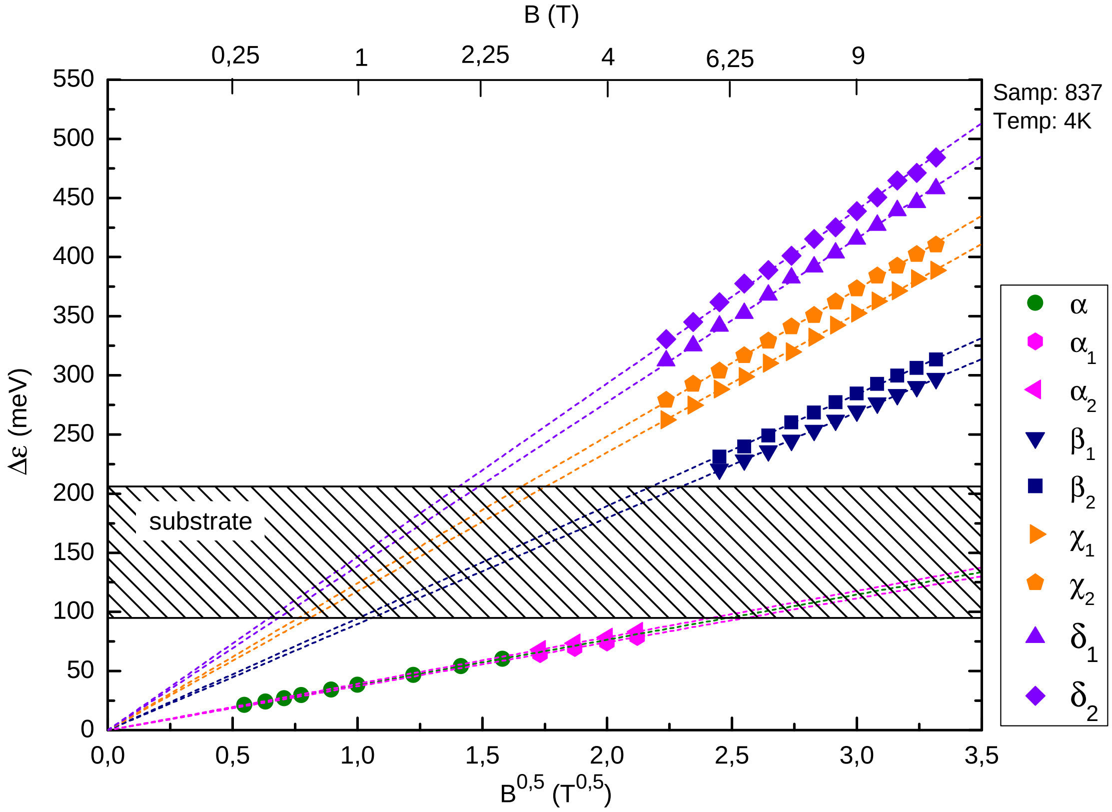

Figure 14: We can see the energies $\Delta\varepsilon$ of various transitions as a function of $\sqrt{B}$ for the sample 837. The dotted lines are linear fits, giving the values for the Fermi velocity $\tilde{c}$.

4.3 Raman scattering studies

We performed Raman scattering on the sample 837, before and after peeling it with a tape, and on the tape itself. We used a confocal microscope with 2μm spatial and 1nm spectral resolution, a HeNe laser with a line at 632.8nm and measured at room temperature. Since the three spectra, presented in figure 15, were made of different flakes on the sample, their intensities can not be related to each other. Concerning the energies, where the Stokes line appears, we can see for the sample, before and after peeling, a Raman spectrum of few layer graphene on the C face of silicon carbide (FLG-C-SiC)[6]. The line at 1580 cm^{-1}, called G band, corresponds to the first order (one phonon) Raman scattering. It is due to the in-plane optical phonon E_{2g} of the sp^2 hybridisation in the lattice structure. The D' band at 2655 cm^{-1} corresponds to the second order (double phonon) Raman scattering and is due to zone boundary phonons. Both lines are superposed with the characteristic intensity shape of the SiC Raman spectra. After peeling we can clearly see a decrease in intensity of the G and D' band with respect to the intensity of the SiC phonons. Because the two spectra have been made on different flakes, this decrease does not really imply, that this is related to exfoliated layers. But since the epitaxial growing provides a consistent growth on the substrate in a certain range, we can assume that we made the spectrum on a flake, where layers have been peeled away. The Raman spectrum of the tape shows the G and D' band at the same wave numbers, but without the background of SiC. In addition, several other peaks appear, due to the tape itself. Whereas the results, presented in [6], show a shift of the D' band of graphene, exfoliated from highly oriented pyrolytic graphite (HOPG) with Bernal stacking, to lower wave numbers, the D' band in the spectrum of our tape remains on the same position. As a result, we can assume to have graphene layers on the tape exfoliated from FLG-C-SiC.

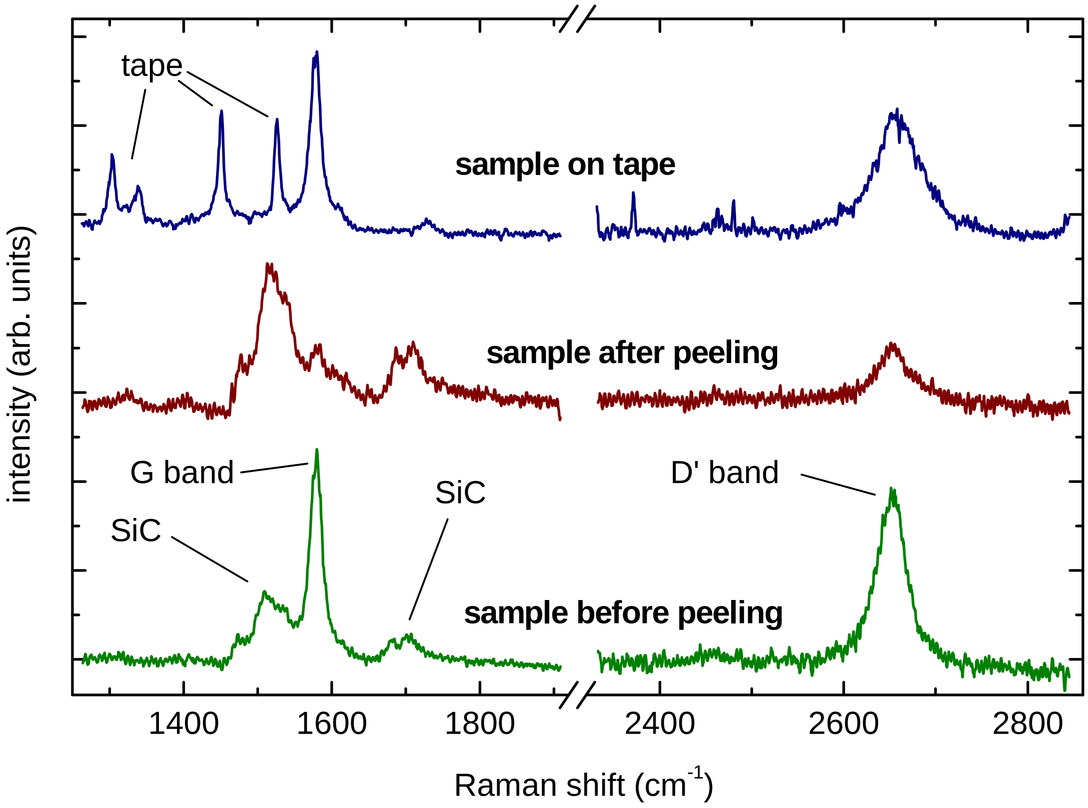

Figure 15: The Raman spectra of the sample 837, before and after peeling with a tape, and the tape itself are presented. The spectra were smoothed with an adjacent averaging and the scale of the intensity differs from spectrum to spectrum, due to baseline corrections.

4.4 Transmittance of the new samples

Since the Raman spectra were promising, we peeled sample 838 as well and measured the transmission in magnetic fields of the exfoliated graphene layers on the tape and the remaining part on the SiC substrate. Unfortunately we were not able to see infrared absorption of the exfoliated graphene, for both samples. One reason could be, that the area on the tape, covered with graphene flakes, is small compared to the whole tape. This is in fact no problem for Raman scattering, since the laser spot has approx. the size of the flakes and can be pointed on them. However, in our transmission measurements, the whole sample is illuminated and therefore most of the light would not pass any graphene layers. This would result in a very low absorption, that probably could not be seen at the given signal to noise ratio. Another reason might be, that the exfoliation induced a large increase in the carrier concentration of the exfoliated graphene layers. Therefore very high magnetic fields are necessary to see transitions absorbing light in the accessible spectral region. We measured the transmission of the tape up to 32T, but could not observe the desired absorption. Though we focused our studies on the epitaxial samples after peeling, which will be denoted by 837p and 837p2, because we peeled a second time, and 838p. When measuring the transmission of 837p, we used the globar, a silicon window for the probe, detected with a silicon window bolometer and worked at 4K. For the spectral region up to 500cm^{-1}, we used the beam splitter M6 and additionally a black polyethylene window as optical filter to cut off the high frequencies. Between

400cm^{-1} and 650cm^{-1} we measured with the KBr beam splitter. For the high energy region, after the absorption band, we used the CaF$_2$ beam splitter. After the second peeling, we measured under the same conditions then before. Spectra in the low field region for magnetic fields between 1T and 3.5T, and for the high field region between 7T and 11T are shown in figure 16. For comparison, the corresponding spectra before peeling are added. In the spectral region above 1750cm^{-1} we can see for the transition β_1 a decrease in absorption of the left peak of 25% at 11T to 40% at 7T, after peeling one time (837p). The right peak vanishes almost and can barely be seen in the spectra. After peeling a second time (837p2) the left peak is decreasing approx. by another 10% and seems to be slightly shifted to lower wave numbers. The transitions χ_1 and δ_1 can still be seen. In the spectral region between 400cm^{-1} and 650cm^{-1} we can see for the transition α_1 a decrease of the left peak from 25% at 3.5T to 40% at 2.5T, for 837p. The noise makes it difficult to notice ay trace of a right peak, but there is no indication for this. The spectra for 837p2 show again a small shift of the left peak. For wave numbers up to 500cm^{-1} the decrease in absorption stays at approx. 40% and the shift of the whole peak has increased. This peak is in fact a superposition of two peaks corresponding to the two different Fermi velocities, measured in the higher spectral range, which are very close to each other. Since the right peak seems to vanish again, as seen at higher frequencies, we can only see the left one, which should be denoted by α_1. The plot for the transition energies $\Delta\varepsilon_{n,|n|\pm1}$ as a function of $\sqrt{B}$ for 837p and 837p2 are shown in figure 17. The Fermi velocities, which are shown in table 3, derived from the higher transitions β_1, χ_1 and δ_1 remain the same for 837p, with respect to the original sample. For 837p2, they are lower, what however is still in the region of the uncertainty. The Fermi velocity, derived from α_1, did not change.

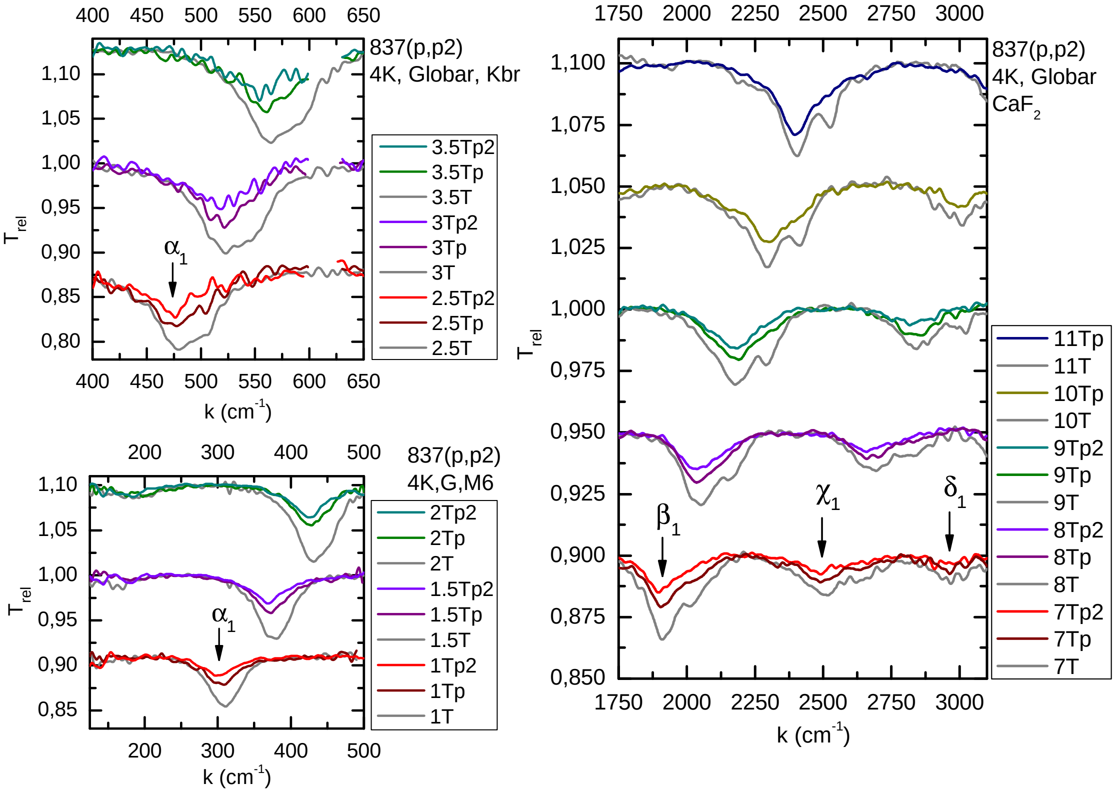

Figure 16: We can see spectra, derived from the samples 837p and 837p2, for various magnetic fields. Some spectra had to be cut due to phonon bands of the silicon window in the beam path. For comparison, the corresponding spectra before peeling are added, shown in grey.

	α_1	β_1	χ_1	δ_1
$\tilde{c}$ (10^6m/s), 837p	1.03	1.03	1.03	1.02
$\tilde{c}$ (10^6m/s), 837p2	1.03	1.02	1.02	1.02

Table 3: The Fermi velocity $\tilde{c}$ derived from individual transitions is presented, with an uncertainty of 2%.

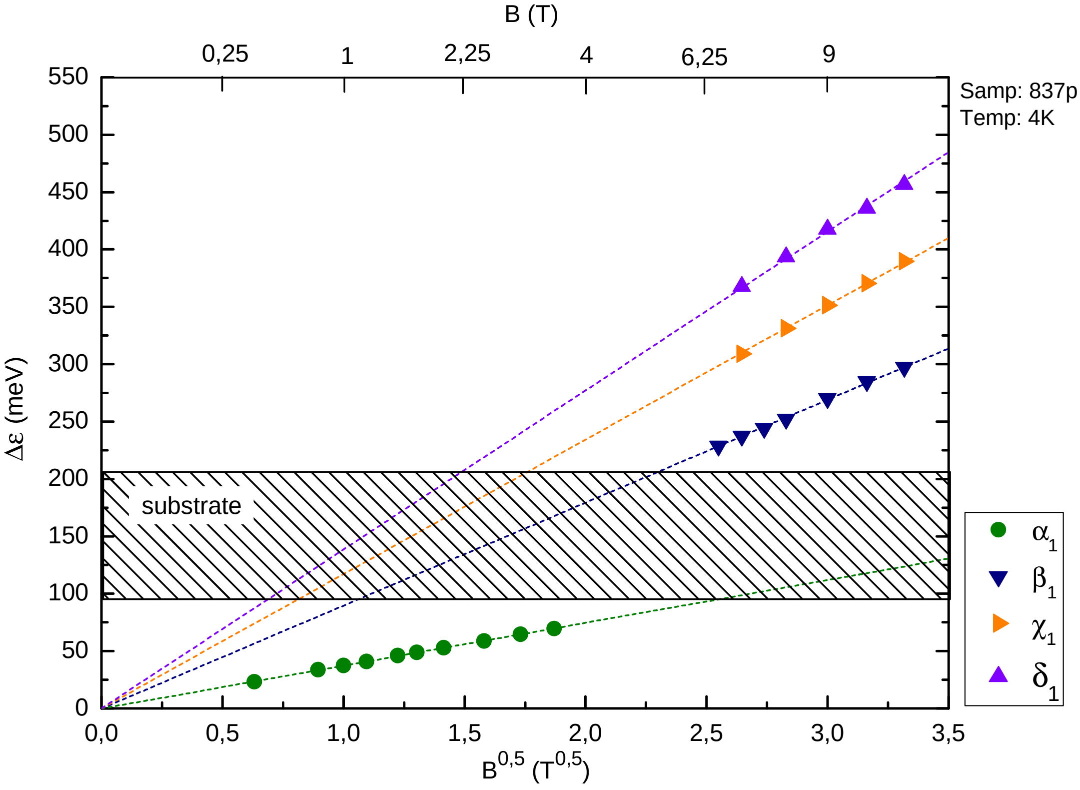

Figure 17: We can see the energies $\Delta\varepsilon$ of various transitions as a function of $\sqrt{B}$ for the peeled sample 837p. The dotted lines are linear fits, giving the values for the Fermi velocity $\tilde{c}$.

In addition, we present a few spectra, derived from the sample 838p. For the transmission measurements in magnetic fields we used the globar light source and worked at 4K. In the spectral region before the absorption band we measured with a polyethylene window bolometer, a polyethylene window for the probe and used up to 500cm^{-1} beam splitter M6, and further KBr. For the spectral region above 1750cm^{-1} we measured with the CaF$_2$ beam splitter, CaF$_2$ window for the probe and a silicon window bolmeter. The spectra are shown in figure 18 and pointed on the spectral region, where the splitting begins to evolve. We can see the transition α_1 between 200cm^{-1} and 680cm^{-1} for fields between 0.8T and 4T, and the corresponding spectra of the sample 838 for comparison. We can clearly notice, that the peak is shifted to lower wave numbers and shows a decrease in intensity of 30% for 4T to 50% for 0.8T. The values for the Fermi velocity are given in table 4. For the transitions β_1, χ_1 and δ_1, we derived the same Fermi velocities as before peeling. The value, derived from α_1 is in agreement with the one for 837p and 837p2.

	α_1	β_1	χ_1	δ_1
$\tilde{c}$ (10^6m/s), 838p	1.02	1.03	1.03	1.03

Table 4: The Fermi velocity $\tilde{c}$ derived from individual transitions is presented, with an uncertainty of 2%.

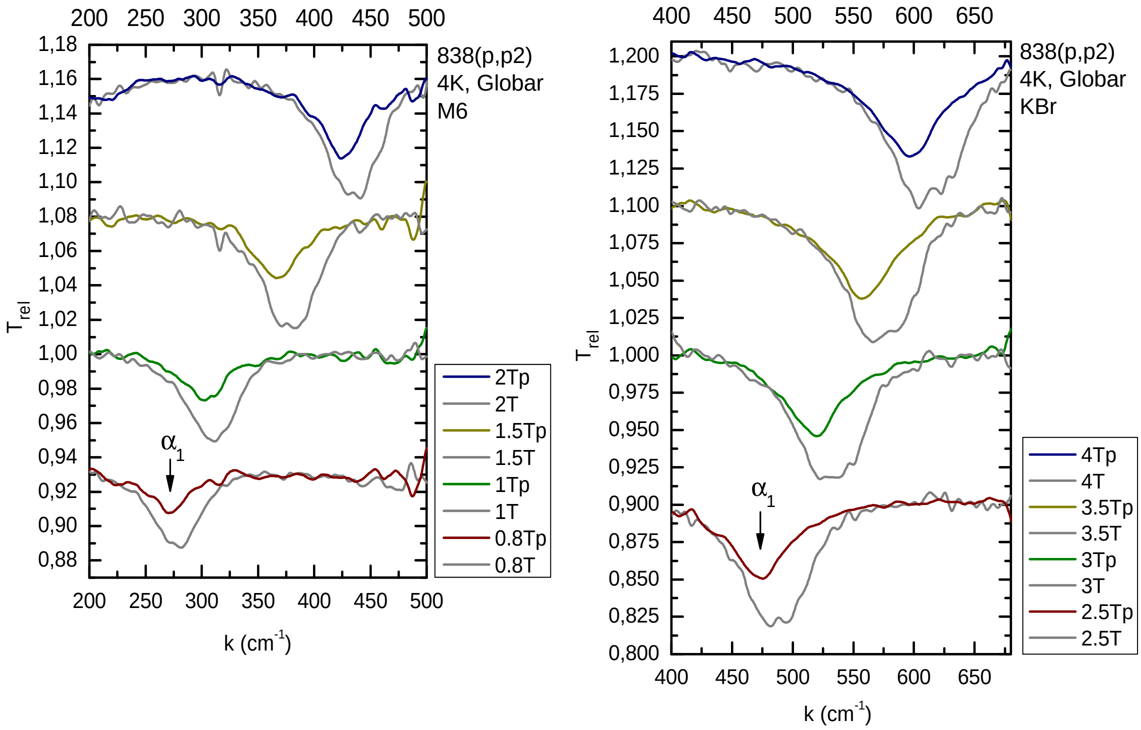

Figure 18: We can see spectra, derived from the sample 838p, for various magnetic fields. For comparison, the corresponding spectra before peeling are added, shown in grey.

4.5 Conclusions

We studied the infrared transmission of different epitaxial graphene samples and could verify the Dirac like behavior of the charge carriers in the vicinity of the Dirac points K and K'. Individual Landau level transitions could be identified and evaluated. In addition, we investigated new properties, which occur in an absorption line splitting, leading to different Fermi velocities. One, with a value of $1.03 \cdot 10^6$m/s, which is in agreement with former studies of epitaxial graphene, and another one with about $1.08 \cdot 10^6$m/s. After peeling the samples, we could identify graphene layers on the epitaxial as well as on the exfoliated part by Raman scattering. Studying the transmission of the remaining epitaxial parts, we observed a disappearance of the absorption peak of the higher Fermi velocity. This can be interpreted, that we peeled some upper layers away, whose electrons were interacting differently with electrons of the remaining layers, what resulted in different velocities. By exfoliating we were expecting to observe the influence of these interactions, but we were not able unfortunately to measure an infrared response on the tape.

As a conclusion, we can say that the behavior of charge carriers in epitaxial graphene is still not fully understood. However, the detailed understanding of the coupling between epitaxial graphene layers may lead to improve the efficiency of graphene based devices which are promising for future electronics.

5 Thanks

My first thanks go to Gérard Martinez and Milan Orlita, who introduced me into the laboratory and supervised my work during the whole stage. I want to thank Gérard for very interesting theoretical discussions and exciting measurements. I want to thank Milan for amazing physical discussions and his professional support and help in the shared challenging experiments. I also want to thank Clément Faugeras, for interesting discussions and of course our collaboration in the Raman scattering studies, and Marek Potemski, our group leader, who was always there to help me with problems or questions. Thanks go also to the PhD students Jan Kunc and Johannes Schneider, and the Master students Tomasz Jakubczyk and Zhaohui Bao, with whom I spend a nice time and had interesting discussions. Further thanks go to the rest of the group Paulina Plochocka, Katarzyna Kowalik and Duncan Maude. Of course, in the end I want to thank Georg Maret, who arranged this hole stage and always supported me.

References

[1] D. S. L. Abergel, Vladimir I. Fal'ko, *Optical and magneto-optical far-infrared properties of bilayer graphene*, Physical Review B 75, 155430 (2007)

[2] T. Ando, *Theory of Electronic States and Transport in Carbon Nanotubes*, Journal of the Physical Society of Japan, Vol 74, No. 3, March, 2005, pp. 777-817.

[3] G. Bastard, *Wave mechanics applied to semiconductor heterostructures*, Monographies de Physique, Le Ulis, France.

[4] Yu. A. Bychkov, G. Martinez, *Magnetoplasmon excitations in graphene for filling factors* $\nu \geq 6$, Physical Review B 77, 125417 (2008).

[5] A. H. Castro Neto, F. Guinea, N. M. R. Peres, K.S. Novoselov, A. K. Geim, *The electric properties of graphene*, Reviews of Modern Physics, September 7, 2007.

[6] C. Faugeras, A. Nerrière, M. Potemski, A. Mahmood, E. Dujardin, C. Berger, W. A. de Heer, *Few-layer graphene on SiC, pyrolotic graphite, and graphene: A Raman scattering study*, Applied Physics Letters 92, 011914 (2008).

[7] S. Heinze, *Infrared Spectroscopy and Cyclotron Resonance in Semiconductor Heterostructures*, LCMI, Grenoble, 2006.

[8] C. Kittel, *Introduction to Solid State Physics*, John Wiley & Sons, Inc., New York, London, Sydney, third corrected printing, June, 1968.

[9] M. Potemski, *Massless Dirac-like fermions in 2D allotropes of carbon : Landau level spectroscopy*, LCMI, Grenoble, 2008.

[10] M. L. Sadowski, G. Martinez, M. Potemski, C. Berger, W. A. de Heer, *Landau Level Spectroscopy of Ultrathin Graphite Layers*, Physical Review Letters 97, 266405 (2006).

[11] M. L. Sadowski, G. Martinez, M. Potemski, C. Berger, W. A. de Heer, *Magneto-spectroscopy of epitaxial graphene*, International Journal of Modern Physics B, Vol.21, Nos. 8 & 9 (2007) 1145-1154, World Scientific Publishing Company.

[12] R. Saito, M. S. Dresselhaus, G. Dresselhaus, *Physical properties of carbon nanotubes*, Imperial College Press, London, 1998.

[13] J. Schneider, *Transport measurements to investigate normal and relativistic carriers in graphite*, LCMI, Grenoble, 2007.